LETTER

doi:10.1038/nature18306

High-efficiency two-dimensional Ruddlesden–Popper perovskite solar cells

Hsinhan Tsai[1,2]*, Wanyi Nie[1]*, Jean-Christophe Blancon[1], Constantinos C. Stoumpos[3,4,5], Reza Asadpour[6], Boris Harutyunyan[4,5], Amanda J. Neukirch[1], Rafael Verduzco[2,7], Jared J. Crochet[1], Sergei Tretiak[1], Laurent Pedesseau[8], Jacky Even[8], Muhammad A. Alam[6], Gautam Gupta[1], Jun Lou[2], Pulickel M. Ajayan[2], Michael J. Bedzyk[4,5], Mercouri G. Kanatzidis[3,4,5] & Aditya D. Mohite[1]

Three-dimensional organic–inorganic perovskites have emerged as one of the most promising thin-film solar cell materials owing to their remarkable photophysical properties[1–5], which have led to power conversion efficiencies exceeding 20 per cent[6,7], with the prospect of further improvements towards the Shockley–Queisser limit for a single-junction solar cell (33.5 per cent)[8]. Besides efficiency, another critical factor for photovoltaics and other optoelectronic applications is environmental stability and photostability under operating conditions[9–15]. In contrast to their three-dimensional counterparts, Ruddlesden–Popper phases—layered two-dimensional perovskite films—have shown promising stability, but poor efficiency at only 4.73 per cent[13,16,17]. This relatively poor efficiency is attributed to the inhibition of out-of-plane charge transport by the organic cations, which act like insulating spacing layers between the conducting inorganic slabs. Here we overcome this issue in layered perovskites by producing thin films of near-single-crystalline quality, in which the crystallographic planes of the inorganic perovskite component have a strongly preferential out-of-plane alignment with respect to the contacts in planar solar cells to facilitate efficient charge transport. We report a photovoltaic efficiency of 12.52 per cent with no hysteresis, and the devices exhibit greatly improved stability in comparison to their three-dimensional counterparts when subjected to light, humidity and heat stress tests. Unencapsulated two-dimensional perovskite devices retain over 60 per cent of their efficiency for over 2,250 hours under constant, standard (AM1.5G) illumination, and exhibit greater tolerance to 65 per cent relative humidity than do three-dimensional equivalents. When the devices are encapsulated, the layered devices do not show any degradation under constant AM1.5G illumination or humidity. We anticipate that these results will lead to the growth of single-crystalline, solution-processed, layered, hybrid, perovskite thin films, which are essential for high-performance opto-electronic devices with technologically relevant long-term stability.

The crystal structures of the Ruddlesden–Popper layered perovskites used in this study, $(BA)_2(MA)_2Pb_3I_{10}$ ($n=3$) and $(BA)_2(MA)_3Pb_4I_{13}$ ($n=4$), are illustrated in Fig. 1a. Both are members of the $(BA)_2(MA)_{n-1}Pb_nI_{3n+1}$ layered perovskite family, where $\{(MA)_{n-1}Pb_nI_{3n+1}\}^{2-}$ denotes the anionic layers derived from the parent 3D perovskite, methylammonium lead triiodide ($MAPbI_3$). The anionic layers are isolated from one another by means of the organic *n*-butylammonium (BA) spacer cations. Within the series, the thickness of each perovskite layer can be incrementally adjusted by careful control of the stoichiometry. Here we focus on the $n=4$ member (Fig. 1a, lower panel) unless otherwise stated.

The layered perovskite thin films were fabricated using a hot-casting technique (see Methods for details)[18]. Briefly, the spin coating of the perovskite precursors was performed on a preheated substrate (fluorine-doped tin oxide (FTO)/poly(3,4-ethylenedioxythiophene) polystyrene sulfonate (PEDOT:PSS)). The temperature of the substrate was varied from room temperature to 150 °C, as illustrated in the images shown in Fig. 1b. The hot-cast films look uniform and reflective, suggesting that the film is ideal for fabrication of planar devices. Atomic force microscopy (AFM) and scanning electron microscopy (SEM) were used to compare the morphologies between room-temperature-cast and hot-cast films (Extended Data Fig. 1a–d). From the AFM images, the hot-cast films show substantially larger grains (about 400 nm) in comparison to the room-temperature spin-coated films (about 150 nm), resulting in a much more compact and uniform thin film. SEM images further confirm the much lower density of pinholes in the hot-cast films in comparison to RT cast films. The presence of pinholes makes it challenging to fabricate working planar-type devices.

We further investigated the crystallinity of the perovskite films using the grazing incidence X-ray diffraction (GIXRD) technique (Fig. 1c). Three dominant planes were observed at diffraction angles (2θ, Cu K_α) of 14.20°, 28.48° and 43.28°, representing the $(BA)_2(MA)_3Pb_4I_{13}$ crystallographic planes $(\bar{1}1\bar{1})$, (202) and (313), respectively, in both of the films[16]. The full-width at half-maximum (FWHM) as a function of hot-casting temperature for the (202) plane is plotted in Fig. 1d; the FWHM of the (202) plane is greatly reduced from 0.63° to 0.29° when the casting temperature increase from room temperature to 110 °C, and remains constant at 0.27° for higher temperatures. The diffraction background and FWHM for each plane are also reduced for the hot-cast film (Fig. 1c and Fig. 1d inset). These results suggest that the crystallinity of the hot-cast films is superior to that of the room-temperature-cast films and becomes optimal at 110 °C. This stark difference in the observed GIXRD patterns motivated in-depth crystallography measurements using grazing incidence wide-angle X-ray scattering (GIWAXS) imaging, and is discussed with reference to Fig. 2.

The optical absorbance and photoluminescence spectra of the perovskite thin films are illustrated in Fig. 1e (see also Extended Data Fig. 2). The photoluminescence and absorption yield band-edge energies of 1.655 ± 0.002 eV and 1.66 ± 0.01 eV, respectively, in good agreement with previous reports[16]. Density functional theory (DFT)

[1]Los Alamos National Laboratory, Los Alamos, New Mexico 87545, USA. [2]Department of Materials Science and Nanoengineering, Rice University, Houston, Texas 77005, USA. [3]Department of Chemistry, Northwestern University, Evanston, Illinois 60208, USA. [4]Department of Materials Science, Northwestern University, Evanston, Illinois 60208, USA. [5]Engineering and Argonne-Northwestern Solar Energy Research (ANSER) Center, Northwestern University, Evanston, Illinois 60208, USA. [6]School of Electrical and Computer Engineering, Purdue University, West Lafayette, Indiana 47907, USA. [7]Department of Chemical and Biomolecular Engineering, Rice University, Houston, Texas 77005, USA. [8]Fonctions Optiques pour les Technologies de l'Information, FOTON UMR 6082, CNRS, INSA de Rennes, 35708 Rennes, France.
*These authors contributed equally to this work.

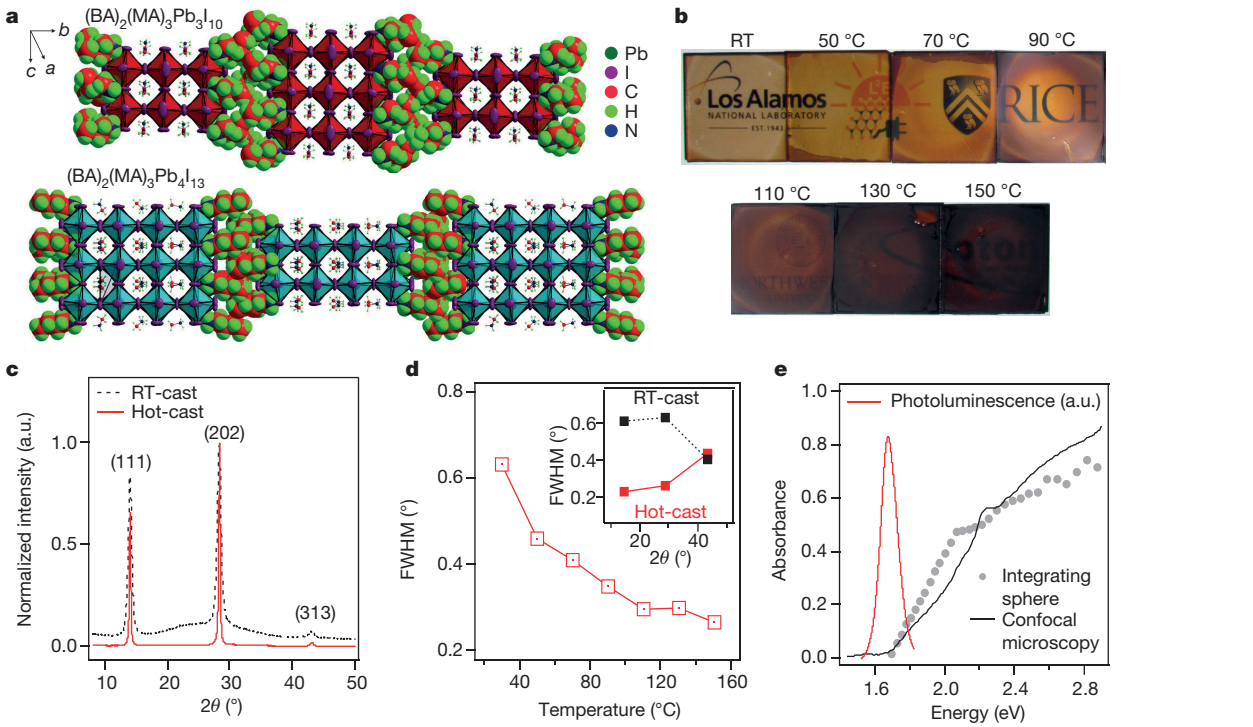

Figure 1 | Crystal structure and thin-film characterization of layered perovskites. a, The crystal structure of the Ruddlesden–Popper $(BA)_2(MA)_2Pb_3I_{10}$ and $(BA)_2(MA)_3Pb_4I_{13}$ layered perovskites, depicted as *n* polyhedral blocks, where *n* refers to the number of layers; the BA spacer layers are depicted as space-fill models to illustrate the termination of the perovskite layers. **b**, Photos of $(BA)_2(MA)_3Pb_4I_{13}$ thin films cast from room temperature (RT) to 150 °C. The film colour gets darker with increasing temperature. **c**, Comparison of GIXRD spectra for room-temperature-cast (black dashed line) and hot-cast (red line) $(BA)_2(MA)_3Pb_4I_{13}$ films, respectively. The (111), (202) and (313) labels correspond to preferred diffraction planes. **d**, The full-width at half-maximum (FWHM) of GIXRD peak (202) as a function of temperature from room temperature to 150 °C. The inset shows the FWHM for each plane indicated in **c**. **e**, Absorbance of a 370-nm thin film ($n = 4$) measured in an integrating sphere (grey circles) and with confocal microscopy (black line), along with the photoluminescence spectra for excitation at 1.96 eV (red line). a.u., arbitrary units.

computations predict that $(BA)_2(MA)_{n-1}Pb_nI_{3n+1}$ compounds have a direct bandgap, with gap energies essentially related to the number of inorganic layers (see Methods, Extended Data Fig. 3 and Supplementary Discussion). The bandgap energy (E_g) can indeed be tuned experimentally from $E_g = 1.52$ eV for $n \to \infty$, similar to 3D $MAPbI_3$, to $E_g = 2.43$ eV for a single atomic layer ($n = 1$), in good agreement with experimental results[12,16,19]. Furthermore, we predict that for $(BA)_2(MA)_2Pb_3I_{10}$ ($n = 3$) and $(BA)_2(MA)_3Pb_4I_{13}$ ($n = 4$) compounds, the exciton binding energy is closer to that of $MAPbI_3$ ($n \to \infty$), for which the excitons are expected to be almost ionized at room temperature and charge-carrier transport is expected to be dominated by free carriers (Supplementary Discussion). These theoretical predictions are in good agreement with the experimentally measured optical absorption spectra, which do not exhibit excitonic signatures (Fig. 1e). Moreover, the apparent lack of Urbach tails in the optical absorption, the very small Stokes shift, and the strong absorption and photoluminescence are indicative that the $(BA)_2(MA)_3Pb_4I_{13}$ perovskite behaves like a direct-bandgap intrinsic semiconductor with excellent crystallinity, very few carrier traps and disorder-induced density of states in the bandgap[20].

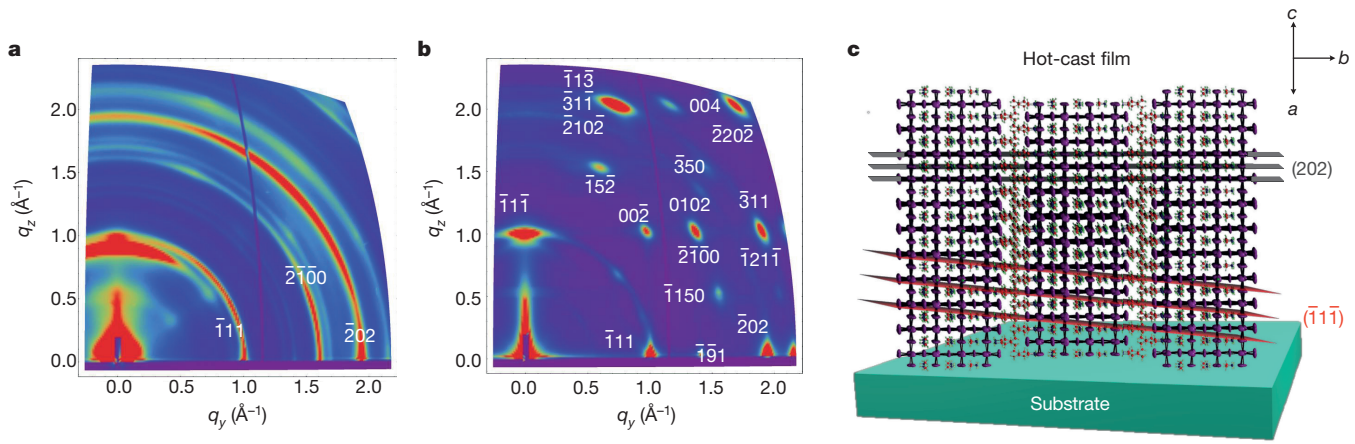

Figure 2 | GIWAXS images and structure orientation. a, **b**, GIWAXS maps for polycrystalline room-temperature-cast (**a**) and hot-cast (**b**) near-single-crystalline $(BA)_2(MA)_3Pb_4I_{13}$ perovskite films with Miller indices of the most prominent peaks shown in white. Colour scale is proportional to X-ray scattering intensity. **c**, Schematic representation of the (101) orientation, along with the $(\bar{1}1\bar{1})$ and (202) planes of a 2D perovskite crystal, consistent with the GIWAXS data.

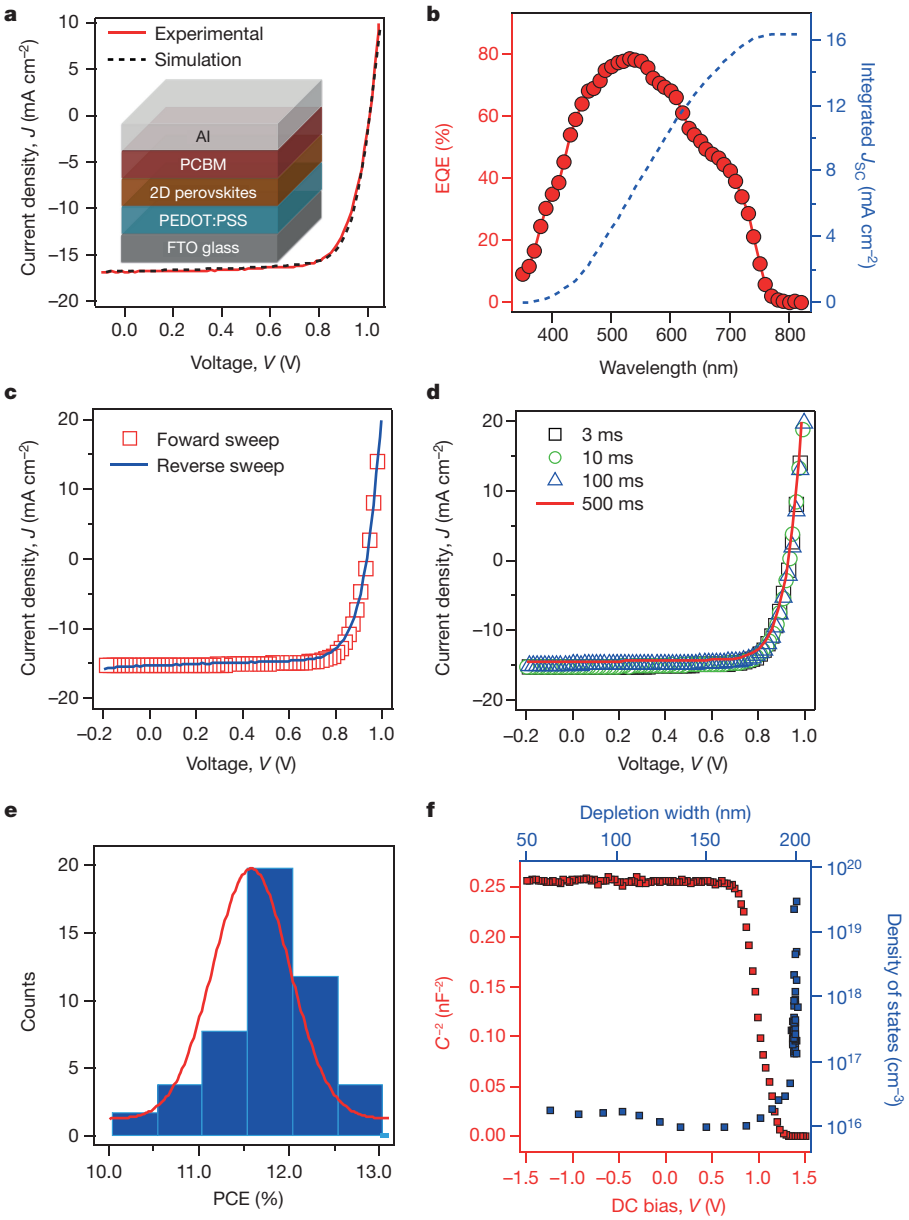

Figure 3 | Solar cell architecture and characterization. a, Experimental (red line) and simulated (black dashed line) current-density–voltage (J–V) curves under an AM.1.5G solar simulator for planar devices using 2D $(BA)_2(MA)_3Pb_4I_{13}$ perovskites as the absorbing layer at optimized thickness (230 nm). The inset shows the device architecture. Al, aluminium; PCBM, [6,6]-phenyl-C61-butyric acid methyl ester; PEDOT:PSS, poly(3,4-ethylenedioxythiophene) polystyrene sulfonate; FTO, fluorine-doped tin oxide. **b**, External quantum efficiency (EQE; red circles and line) and integrated short-circuit current density (J_{SC}; blue dashed line) as a function of wavelength. **c**, **d**, J–V curves for hysteresis tests under AM1.5G illumination measured with the voltage scanned in opposite directions (**c**) and with varying voltage delay times (**d**). **e**, Histogram of $(BA)_2(MA)_3Pb_4I_{13}$ device power conversion efficiency (PCE) over 50 measured devices, fitted with a Gaussian distribution (red line). **f**, Capacitance–d.c. bias (C–V) curves (red squares) for a typical device detected by a small-amplitude a.c. field (peak-to-peak voltage $V_{PP} = 20$ mV) at an a.c. frequency of 100 kHz, and the corresponding charge density profile (blue squares) extracted from the C–V curve.

To probe the perovskite orientation with respect to the substrate in the thin films we performed a GIWAXS analysis using synchrotron radiation (Fig. 2a, b). The resulting scattering patterns reveal two major characteristics for the films. The room-temperature-cast films (Fig. 2a) exhibit diffraction rings with stronger intensities along certain extended arc segments, which indicates considerable randomness in the 3D orientation of the crystal domains (grains) within the polycrystalline film. By contrast, the hot-cast films (Fig. 2b) exhibit sharp, discrete Bragg spots along the same rings, indicating a textured polycrystalline film in which the crystal domains are oriented with their (101) planes parallel to the substrate surface (as shown in Fig. 2c) and with a 2D in-plane orientational randomness. This crystallographic determination came from indexing the observed Bragg peaks in Fig. 2b using a simulated diffraction pattern from the orthorhombic structure described above. It is apparent from the synchrotron diffraction data that the major perovskite growth direction lies along the (101) plane that is parallel to the q_z direction, as illustrated in Fig. 2c and confirmed by the presence of the $(\bar{1}1\bar{1})$ and (202) spots as the most prominent reflections with q_z.

The growth of highly uniform, layered perovskite thin films with excellent crystallinity and optical properties motivates their use in planar photovoltaic devices. Solar cells fabricated with these thin films yield high power-conversion efficiency with robust and reproducible performance (Fig. 3). The experimental and simulated current density versus voltage characteristics measured under standard AM1.5G (air mass 1.5 global 1-Sun) illumination for the device with $(BA)_2(MA)_3Pb_4I_{13}$ deposited using the hot-casting method[18] are illustrated in Fig. 3a (inset shows the planar device structure). We record a peak power conversion efficiency (PCE) of 12.51% with an open circuit voltage $V_{OC} = 1.01$ V, short-circuit current density $J_{SC} = 16.76$ mA cm^{-2} and fill factor of 74.13% using hot-cast films of 2D $(BA)_2(MA)_3Pb_4I_{13}$ perovskite (see Extended Data Fig. 4 for $(BA)_2(MA)_2Pb_3I_{10}$ device performance). We emphasize that in comparison to 3D perovskites ($V_{OC} \approx 0.7$–0.9 V)[15,18,21,22], the layered 2D perovskites provide an opportunity to achieve high V_{OC}, in a simple planar architecture (see Supplementary Discussion and Extended Data Fig. 1e). For comparison, we fabricated the device using the same materials, but using a conventional spin-coating method, and obtained average efficiencies of approximately 3%–4% (Extended Data Fig. 1f), similar to a previous study[16]. The large increase in efficiency is attributed to the increase in J_{SC} and fill factor. We assign this increase to the enhanced charge transport and mobility (Extended Data Fig. 5) facilitated by the near-perfect vertical orientation of the $\{(MA)_{n-1}Pb_nI_{3n+1}\}^{2-}$ slabs as demonstrated in

Fig. 2c, relative to the FTO substrate. The excellent crystallinity and thin-film uniformity that are realized by the hot-casting technique lead to continuous charge-transport channels that enable the highly mobile photo-generated carriers to travel through the two-dimensional $\{(MA)_{n-1}Pb_nI_{3n+1}\}^{2-}$ slabs across device electrodes, without being blocked by the insulating spacer layers. The measured external quantum efficiency (EQE) and the integrated J_{SC} for $(BA)_2(MA)_3Pb_4I_{13}$ are illustrated in Fig. 3b; the EQE spectrum is in good agreement with the optical absorption profile (Fig. 1e and Extended Data Fig. 2). The integrated J_{SC} from the EQE spectrum is calculated to be 16.31 mA cm^{-2} for $(BA)_2(MA)_3Pb_4I_{13}$, which is within 3% of the J_{SC} measured under AM1.5G standard irradiation. We also performed a film-thickness optimization for solar cell performance using $(BA)_2(MA)_3Pb_4I_{13}$ in the same device geometry by varying the molar concentration of the solution (0.9 M to 0.115 M based on total Pb^{2+}) and found that J_{SC} was optimal for a film thickness of approximately 230 nm. Although thicker films enhance light harvesting, the charge transport limits the overall efficiency (see Extended Data Fig. 6). We also tested these devices for the detrimental hysteresis effect that has been reported in conventional 3D hybrid perovskite[23–25]. Figure 3c, d illustrates the current density as a function of applied voltage, for different sweep directions and voltage delay times, respectively. In contrast to previous reports[13,16], no hysteresis was observed in either case. In fact, these devices demonstrate excellent reproducibility with an average efficiency of 11.60% ± 0.92% over 50 devices, as illustrated through the statistical distribution presented in Fig. 3e.

To rationalize the remarkable reproducibility and the lack of hysteresis of these devices, we performed capacitance–voltage (C–V) measurements and extracted the charge density profile (Fig. 3f) using the Mott–Schottky equation in the reverse bias regime[26–28] (see Supplementary Discussion). From the C–V curve (Fig. 3f, bottom and left axes), it is clear that the device is fully depleted, and the trap density is quite small to substantially affect the J–V characteristics through trapped charges. The device behaves like a p–i–n junction, where layered perovskite acts as an intrinsic semiconductor. The total charge density in the depletion region was calculated to be 10^{16} cm^{-3} (Fig. 3f, top and right axes)[28,29]. Moreover, the calculated edge of the depletion region, where the charge density becomes flat (about 200 nm), is comparable to the film thickness, which indicates that the built-in field is strong enough to extract the charges effectively, leading to a very efficient device. With a fully depleted junction, the C–V curve for the device is not affected by the direction of the voltage scan (see Extended Data Fig. 7a), owing to the lack of trap states, consistent with the observation of hysteresis-free J–V curves.

We performed a self-consistent optoelectronic simulation (involving the solution of Maxwell, Poisson and drift-diffusion equations) to examine the hypothesis of improved material quality when using the hot-cast method. Material parameters are summarized in Supplementary Discussion, with the defect density and mobility being used as the fitting parameters; however, the fitted defect density is in the range of the measured charge density (see Fig. 3f). Extended Data Fig. 8 shows that the simulation results are in good agreement with experimental data, and that they reproduce the general features of the J–V characteristic of both the hot-cast (12.52% efficiency) and room-temperature-cast (4.44% efficiency) solar cells. The increase in efficiency can be attributed to mobility improvement, reduced defect density and improved series resistance.

We performed aggressive long-term stability measurements on the layered 2D and 3D perovskite devices and thin films (Fig. 4). First, we compared the stability of the devices under constant light illumination (AM1.5G), without any encapsulation layer (see Fig. 4a, b and Methods for details). Figure 4a shows the normalized power conversion efficiency as a function of testing time under constant AM1.5G illumination. The PCE of the 3D perovskite device degrades to 40% of its original value within the first 24 h, followed by slow degradation to <10% of its original value over the next 2,250 h (about 94 days). This result is consistent with reports of same device structure and testing conditions[11,15]. In contrast, the 2D device retained 80% of its original PCE after 200 h and slowly degraded to about 70% after another 2,050 h.

Second, we performed a humidity test on the devices by placing the unencapsulated solar cells in a humidity chamber (with a relative humidity of 65%). Figure 4b shows the normalized PCE as a function of testing time, under 65% relative humidity, for the 2D and 3D perovskite devices. The 3D perovskite devices undergo a marked degradation within the first 10 h of exposure. This degradation is expected, owing to the hygroscopic nature of the MA cation and the PEDOT layer. The unencapsulated 2D perovskite devices also show degradation, but at a much slower rate in comparison to the 3D perovskite devices. We speculate that the slower degradation could be due to the long and bulkier hydrophobic organic side group in the 2D perovskite structure that, to a large degree, can prevent (or delay) the direct exposure to moisture and thus increase its threshold against degradation.

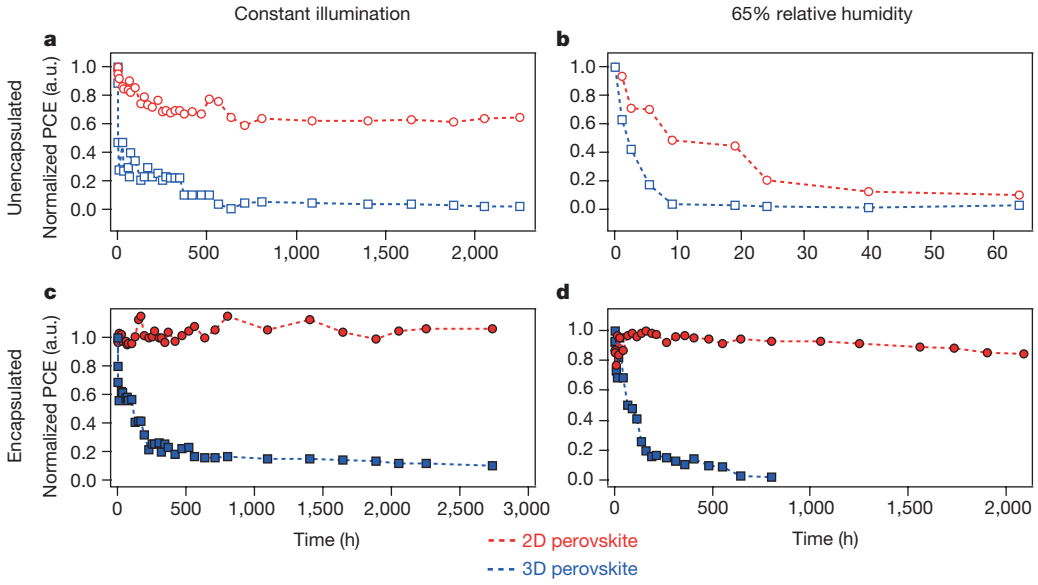

Figure 4 | Stability measurements on planar solar cells. **a**, **c**, Photostability tests under constant AM1.5G illumination for 2D ($(BA)_2(MA)_3Pb_4I_{13}$; red) and 3D ($MAPbI_3$; blue) perovskite devices without (**a**) and with (**c**) encapsulation. **b**, **d**, Humidity stability tests under 65% relative humidity at in a humidity chamber for 2D ($(BA)_2(MA)_3Pb_4I_{13}$; red) and 3D ($MAPbI_3$; blue) perovskite devices without (**b**) and with (**d**) encapsulation. PCE, power conversion efficiency; a.u., arbitrary units.

Finally, we performed the same set of stability tests (under light or humidity) on the 2D and 3D devices with simple glass encapsulation with a UV-curable epoxy resin. Figure 4c, d shows the normalized PCE for encapsulated 2D and 3D perovskite devices tested under constant AM1.5G illumination and 65% humidity for over 2,250 h. Under light stress (Fig. 4c), the PCE degraded to about 50% of its original value within the first 10 h in the 3D device (similar to the unencapsulated 3D device as shown in Fig. 4a), progressively degraded at a very slow rate over the next 800 h and then saturated at approximately 10% of its original value. In contrast, the 2D encapsulated perovskite devices were found to be extremely robust, with no degradation and negligible hysteresis (Extended Data Fig. 7b–d) over 2,250 h of constant light stressing (Fig. 4c). From the light stress tests for the 3D perovskites, we conclude that the observed degradation in the first 10 h in the encapsulated and unencapsulated devices is similar, and so is independent of encapsulation, suggesting that the degradation is a light-activated process.

The humidity stress test for the encapsulated devices (Fig. 4d) reveals that the degradation rate of the PCE for 3D perovskites is much slower than for unencapsulated devices (Fig. 4b), but that the PCE still decreases to $<10\%$ of its original value over 350 h. By contrast, the encapsulated 2D devices do not exhibit any degradation in the first 650 h, representing a substantial slowing down of the degradation in humidity.

These stress tests demonstrate that the 2D layered perovskite devices are stable over long-term operation against light soaking and humidity (see heat stress test in Supplementary Discussion and Extended Data Fig. 9), in contrast to 3D perovskite devices. These results reinforce the importance of encapsulation schemes, and motivate the use of design strategies[9,30,31] such as the addition of metal oxide layers onto 3D perovskites to improve charge transport and the encapsulation of layered 2D perovskite devices for long-term stability.

Online Content Methods, along with any additional Extended Data display items and Source Data, are available in the online version of the paper; references unique to these sections appear only in the online paper.

Received 29 October 2015; accepted 3 May 2016.
Published online 6 July 2016.

1. Yaffe, O. *et al.* Excitons in ultrathin organic-inorganic perovskite crystals. *Phys. Rev. B* **92,** 045414 (2015).
2. Wang, G. *et al.* Wafer-scale growth of large arrays of perovskite microplate crystals for functional electronics and optoelectronics. *Sci. Adv.* **1,** e1500613 (2015).
3. de Quilettes, D. W. *et al.* Impact of microstructure on local carrier lifetime in perovskite solar cells. *Science* **348,** 683–686 (2015).
4. Yin, W.-J., Shi, T. & Yan, Y. Unique properties of halide perovskites as possible origins of the superior solar cell performance. *Adv. Mater.* **26,** 4653–4658 (2014).
5. Stranks, S. D. *et al.* Electron-hole diffusion lengths exceeding 1 micrometer in an organometal trihalide perovskite absorber. *Science* **342,** 341–344 (2013).
6. Saliba, M. *et al.* A molecularly engineered hole-transporting material for efficient perovskite solar cells. *Nat. Energy* **1,** 15017 (2016).
7. Yang, W. S. *et al.* High-performance photovoltaic perovskite layers fabricated through intramolecular exchange. *Science* **348,** 1234–1237 (2015).
8. Shockley, W. & Queisser, H. J. Detailed balance limit of efficiency of *p-n* junction solar cells. *J. Appl. Phys.* **32,** 510–519 (1961).
9. You, J. *et al.* Improved air stability of perovskite solar cells via solution-processed metal oxide transport layers. *Nat. Nanotechnol.* **11,** 75–81 (2016).
10. Li, X. *et al.* Improved performance and stability of perovskite solar cells by crystal crosslinking with alkylphosphonic acid ω-ammonium chlorides. *Nat. Chem.* **7,** 703–711 (2015).
11. Kaltenbrunner, M. *et al.* Flexible high power-per-weight perovskite solar cells with chromium oxide–metal contacts for improved stability in air. *Nat. Mater.* **14,** 1032–1039 (2015).
12. Han, Y. *et al.* Degradation observations of encapsulated planar $CH_3NH_3PbI_3$ perovskite solar cells at high temperatures and humidity. *J. Mater. Chem. A Mater. Energy Sustain.* **3,** 8139–8147 (2015).
13. Smith, I. C., Hoke, E. T., Solis-Ibarra, D., McGehee, M. D. & Karunadasa, H. I. A layered hybrid perovskite solar-cell absorber with enhanced moisture stability. *Angew. Chem. Int. Ed.* **53,** 11232–11235 (2014).
14. Noh, J. H., Im, S. H., Heo, J. H., Mandal, T. N. & Seok, S. I. Chemical management for colorful, efficient, and stable inorganic–organic hybrid nanostructured solar cells. *Nano Lett.* **13,** 1764–1769 (2013).
15. Leijtens, T. *et al.* Overcoming ultraviolet light instability of sensitized TiO_2 with meso-superstructured organometal tri-halide perovskite solar cells. *Nat. Commun.* **4,** 2885 (2013).
16. Cao, D. H., Stoumpos, C. C., Farha, O. K., Hupp, J. T. & Kanatzidis, M. G. 2D homologous perovskites as light-absorbing materials for solar cell applications. *J. Am. Chem. Soc.* **137,** 7843–7850 (2015).
17. Kagan, C. R., Mitzi, D. B. & Dimitrakopoulos, C. D. Organic-inorganic hybrid materials as semiconducting channels in thin-film field-effect transistors. *Science* **286,** 945–947 (1999).
18. Nie, W. *et al.* High-efficiency solution-processed perovskite solar cells with millimeter-scale grains. *Science* **347,** 522–525 (2015).
19. Stoumpos, C. C. *et al.* Ruddlesden–Popper hybrid lead iodide perovskite 2D homologous semiconductors. *Chem. Mater.* **28,** 2852–2867 (2016).
20. Sadhanala, A. *et al.* Preparation of single-phase films of $CH_3NH_3Pb(I_{1-x}Br_x)_3$ with sharp optical band edges. *J. Phys. Chem. Lett.* **5,** 2501–2505 (2014).
21. Liang, P.-W. *et al.* Additive enhanced crystallization of solution-processed perovskite for highly efficient planar-heterojunction solar cells. *Adv. Mater.* **26,** 3748–3754 (2014).
22. Jeon, Y.-J. *et al.* Planar heterojunction perovskite solar cells with superior reproducibility. *Sci. Rep.* **4,** 6953 (2014).
23. Tress, W. *et al.* Understanding the rate-dependent *J–V* hysteresis, slow time component, and aging in $CH_3NH_3PbI_3$ perovskite solar cells: the role of a compensated electric field. *Energy Environ. Sci.* **8,** 995–1004 (2015).
24. Unger, E. L. *et al.* Hysteresis and transient behavior in current–voltage measurements of hybrid-perovskite absorber solar cells. *Energy Environ. Sci.* **7,** 3690–3698 (2014).
25. Snaith, H. J. *et al.* Anomalous hysteresis in perovskite solar cells. *J. Phys. Chem. Lett.* **5,** 1511–1515 (2014).
26. Wang, W. *et al.* Device characteristics of CZTSSe thin-film solar cells with 12.6% efficiency. *Adv. Energy Mater.* **4,** 1301465 (2014).
27. Decock, K. *et al.* Defect distributions in thin film solar cells deduced from admittance measurements under different bias voltages. *J. Appl. Phys.* **110,** 063722 (2011).
28. Hegedus, S. S. & Shafarman, W. N. Thin-film solar cells: device measurements and analysis. *Prog. Photovolt. Res. Appl.* **12,** 155–176 (2004).
29. Eisenbarth, T., Unold, T., Caballero, R., Kaufmann, C. A. & Schock, H.-W. Interpretation of admittance, capacitance-voltage, and current-voltage signatures in $Cu(In,Ga)Se_2$ thin film solar cells. *J. Appl. Phys.* **107,** 034509 (2010).
30. Chen, W. *et al.* Efficient and stable large-area perovskite solar cells with inorganic charge extraction layers. *Science* **350,** 944–948 (2015).
31. Mei, A. *et al.* A hole-conductor–free, fully printable mesoscopic perovskite solar cell with high stability. *Science* **345,** 295–298 (2014).

Supplementary Information is available in the online version of the paper.

Acknowledgements This work at LANL was LANL LDRD programme (A.D.M., G.G., J.-C.B. and S.T.). Work at Northwestern University was supported as part of the ANSER Center, an Energy Frontier Research Center funded by the US Department of Energy, Office of Science, Office of Basic Energy Sciences, under Award No. DE-SC0001059. Use of the Advanced Photon Source at Argonne National Laboratory was supported by the US Department of Energy, Office of Science, Office of Basic Energy Sciences, under Contract No. DE-AC02-06CH11357. Work at INSA de Rennes was performed using high-performance computational resources from the French national centres (GENCI/CINES/IDRIS grant 2015-c2012096724), Cellule Energie du CNRS (SOLHYBTRANS Project) and the University of Rennes 1 (Action Incitative,Défis Scientifique Emergents 2015). J.E.'s work is also supported by the Fondation d'entreprises banque Populaire de l'Ouest (Grant PEROPHOT 2015). The work at Purdue University was supported by the Bay Area PV Consortium (a Department of Energy project with Prime Award number DE-EE0004946). This work at LANL was done in part at the Center for Nonlinear Studies (CNLS) and the Center for Integrated Nanotechnologies (CINT). R.V. acknowledges the support of the NSF DMR-1352099.

Author Contributions A.D.M., H.T., W.N. and M.G.K. conceived the idea. H.T., W.N. and A.D.M. designed the experiments, analysed the data and wrote the paper. H.T. fabricated the devices along with W.N. and performed the measurements. J.-C.B. performed optical spectroscopy measurements and analysed the data under the supervision of J.J.C. C.C.S. synthesized the layered perovskites under the supervision of M.G.K. and co-wrote the paper. R.V. arranged the synchrotron experiments data, and B.H. and M.J.B. analysed and indexed the synchrotron XRD data along with M.G.K. J.E., G.G., L.P. and S.T. performed the molecular dynamics simulations. J.E. analysed the data and provided insight in writing the paper. G.G., J.L. and P.M.A. provided insights into the crystal growth of layered perovskites. R.A. and M.A.A. performed the device simulations. A.J.N. performed DFT calculations on layered perovskites under the supervision of S.T. All authors discussed the results and wrote the paper.

Author Information Reprints and permissions information is available at www.nature.com/reprints. The authors declare no competing financial interests. Readers are welcome to comment on the online version of the paper. Correspondence and requests for materials should be addressed to A.D.M. (amohite@lanl.gov).

Reviewer Information *Nature* thanks H. Snaith and the other anonymous reviewer(s) for their contribution to the peer review of this work.

METHODS

Materials and instruments. PEDOT:PSS, methylamine hydrochloride (MACl), methylamine solution (MA, 40% in H_2O), hydriodic acid (HI, 57 wt% in H_2O), hypophosphorous acid (H_3PO_2, 50% in H_2O), lead oxide, butylammine (BA, 99%) and *N*,*N*-dimethylformamide (DMF, anhydrous) were purchased from Sigma-Aldrich. All the materials were used as received without further purification. The light source was a simulated AM1.5G irradiance of 100 mW cm^{-2}; calibration was done using a NIST-certified monocrystalline Si solar cell (Newport 532 ISO1599). The scanning electron micrographs were obtained from FEI 400 F with 10 KeV and a spot size of 3.5; AFM images were collected from Bruker Multimode 8.

Materials synthesis. Raw 2D perovskite materials were prepared by combining PbO, MACl and BA in appropriate ratios in a HI/H_3PO_2 solvent mixture as described previously. A detailed experimental procedure is reported in ref. 16.

Materials preparation and device fabrication. Pb_3I_{10} and Pb_4I_{13} were prepared with molar concentrations of 1.8 M, 0.9 M, 0.45 M, 0.225 M and 0.118 M of Pb^{2+} cations in anhydrous DMF. FTO/PEDOT:PSS substrates were prepared following refs 18,32. FTO glasses were cleaned using an ultra-sonication bath in soap water and rinsed progressively with distilled water, acetone and isopropyl alcohol, and finally treated with oxygen plasma for 3 min. The PEDOT:PSS layer was then spin-coated onto the FTO substrates at 5,000 r.p.m. for 45 s as a hole-transporting layer. The coated substrates were then transferred to an argon-filled glovebox for device fabrication. The 2D perovskite solution was prepared by dissolving 0.025 mM 2D perovskite single crystal in DMF. The solution was then heated under continuous stirring at 70 °C for 30 min before device fabrication. For the film hot-casting process, the FTO/PEDOT:PSS substrates were first preheated from 30 °C to 150 °C on a hot plate for 10 min, right before spin-coating. These were immediately (within 5 s) transferred to the hot FTO/PEDOT:PSS substrates on the spin-coated 'chunk' (which is at room temperature), and 80 µl of precursor solution was dropped onto the hot substrate. The spin-coater was immediately started with a spin speed of 5,000 r.p.m. for 20 s without ramp; the colour of the thin film turned from pale yellow to brown in few seconds as the solvent escaped. After the spin-coater stopped, the substrates were quickly removed from it. The [6,6]-phenyl-C61-butyric acid methyl ester (PCBM) solution was prepared by dissolving 20 mg PCBM in 1 ml chlorobenzene. 50 µl of the PCBM solution was then dropped onto the perovskite-coated FTO/PEDOT substrate and spin-coated at 1,000 r.p.m. for 60 s to form a thin, electron-transporting layer. The metal electrodes (Al and Au) were deposited using a thermal evaporator with a shadow mast with a working area of 0.5 cm^2. GIWAXS measurements were carried out on Sector 8-ID-E at the Advanced Photon Source, Argonne National Laboratory.

Derivation of the perovskite orientation from GIWAXS. The unit vector $\hat{\boldsymbol{n}}$ normal to substrate surface was defined in the lattice reference frame. Finding the orientation of the crystallites (which are rotationally random around $\hat{\boldsymbol{n}}$) amounts to finding the Miller indices of the plane perpendicular to $\hat{\boldsymbol{n}}$. Two peaks were chosen whose possible set of indices can be inferred from powder diffraction patterns. For each peak of the pair (peaks at q_y and q_z directions), an equations was set: $\frac{\hat{\boldsymbol{n}}\cdot\boldsymbol{G}}{G}=\cos(\theta)\equiv\frac{q_z}{q}$, where $\boldsymbol{G}$ is the reciprocal lattice vector for the chosen peak and θ is the angle between the total wavevector transfer $\boldsymbol{q}$ and its z-axis component q_z (both deduced from peak positions on the GIWAXS pattern, q through the relation $q=\sqrt{q_x^2+q_y^2+q_z^2}$). The obtained system of two equations is solved for the Miller indices of the plane, which has as its normal the $\hat{\boldsymbol{n}}$ unit vector. The peak pair that produced the GIWAXS pattern simulation (performed using the Laue condition $\boldsymbol{G}=\boldsymbol{q}$) best matching the experimental pattern was taken as the optimal solution. The Miller plane parallel to the substrate was deduced to be the (101) plane.

Mobility measurement. We measured the mobility using the charge extraction by linearly increasing voltage (CELIV) technique for the hot-cast and room-temperature-cast devices in the same device geometry. The device is connected to a function generator from the FTO side for negative bias with increasing magnitude, and the current transient is recorded by measuring the voltage drop through a resistor (50 Ω) connected in series with the cathode side of the device.

***C–V* measurement.** We performed *C*–*V* measurements on the 2D layered perovskite device to characterize the its charge density profile, as shown in Fig. 3f, in which C^{-2} is plotted against d.c. voltage. The corresponding charge density profile was extracted from Fig. 4 using the standard Mott–Schottky equation[33]:

$$C^{-2}=\frac{2(V_{bi}-V)}{A^2 q\varepsilon_0\varepsilon N}$$

in which V_{bi} is the built-in voltage, A is the device area, q is the elementary charge, ε is the dielectric constant, ε_0 is the vacuum permittivity and N is the charge density. The charge density profile is extracted from the voltage range 0.5 V to −1 V (reverse bias regime), in which there is no d.c. carrier injection and the device behaves as a capacitor. To understand the origin of hysteresis in these devices, we performed *C*–*V* measurements on the 2D devices and measured the charge density profile of the perovskite depletion region in the reverse bias regime from −1.0 V to 0 V (low dark current without charge injection) using the Mott–Schottky equation[33].

Environmental stability test. We first prepared the 2D and 3D perovskites devices in the same device configuration as described in inset of Fig. 3a, with and without encapsulation, by sealing the active area with glass and ultraviolet curable epoxy. For light stress tests, the 2D and 3D perovskite devices were placed under constant AM1.5G illumination, but were taken out from under the light for each *J*–*V* curve scan. For humidity stress tests, the 2D and 3D perovskite devices were placed inside the humidity chamber connected with a desiccant and a humidifier to control the relative humidity (65%); the relative humidity values were calibrated with two digital humidity sensors at two corners of the chamber.

32. Tsai, H. *et al.* Optimizing composition and morphology for large-grain perovskite solar cells via chemical control. *Chem. Mater.* **27,** 5570–5576 (2015).
33. Gelderman, K., Lee, L. & Donne, S. W. Flat-band potential of a semiconductor: using the Mott–Schottky equation. *J. Chem. Educ.* **84,** 685–688 (2007).
34. Schulz, P. *et al.* Interface energetics in organo-metal halide perovskite-based photovoltaic cells. *Energy Environ. Sci.* **7,** 1377–1381 (2014).
35. Brivio, F., Walker, A. B. & Walsh, A. Structural and electronic properties of hybrid perovskites for high-efficiency thin-film photovoltaics from first-principles. *APL Mater.* **1,** 042111 (2013).
36. Trukhanov, V. A., Bruevich, V. V. & Paraschuk, D. Y. Effect of doping on performance of organic solar cells. *Phys. Rev. B* **84,** 205318 (2011).

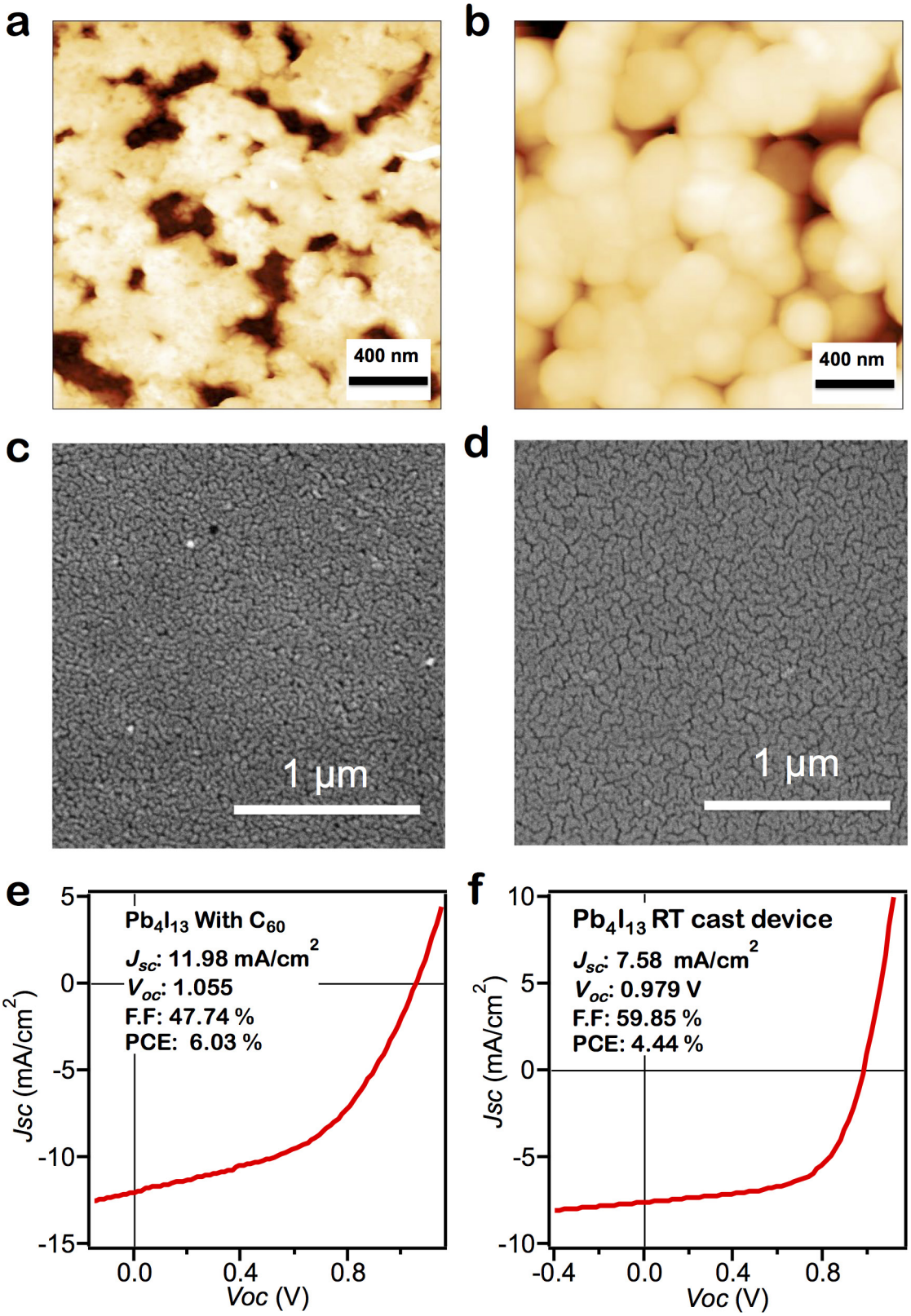

Extended Data Figure 1 | Layered perovskite thin-film morphology and device performance. a, **b**, AFM images of surface morphology for room-temperature-cast (**a**) and hot-cast (**b**) films. Scale bars, 400 nm. **c**, **d**, SEM images of topography for room-temperature-cast (**c**) and hot-cast (**d**) films. Scale bars, 1 μm. **e**, *J*–*V* curve of Pb_4I_{13} with C_{60} as a contact modification candidate shows the enhancement of V_{OC} from 0.9 V to 1.055 V with the same device architecture. **f**, *J*–*V* curve for the $(BA)_2(MA)_3Pb_4I_{13}$ device using the room-temperature (RT) spin-cast method. FF, fill factor.

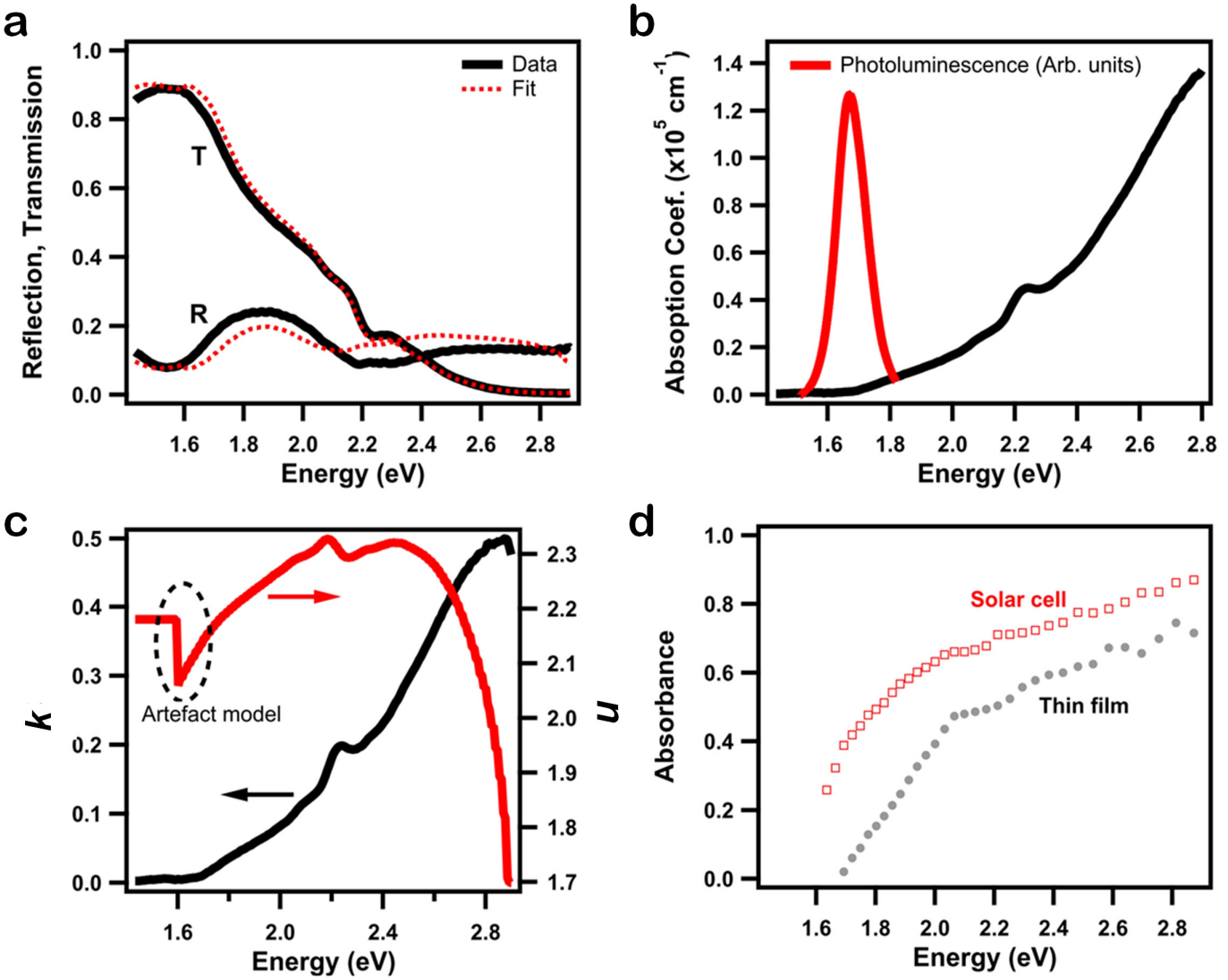

Extended Data Figure 2 | Absorption spectroscopy of layered 2D perovskites. a–c, Local optical absorption characteristics of thin films using reflection/transmission experimental methods (see also refs 34,35 for details of the modelling): results of the fitting of the reflection (R) and transmission (T) data (**a**); absolute absorption cross-section (**b**); and real (n; red line) and imaginary (k; black line) parts of the refractive index (**c**). **d**, Absorbance of thin films (grey circles) compared to that of optimized solar cells (red squares) measured using integrating sphere techniques (see details in ref. 36).

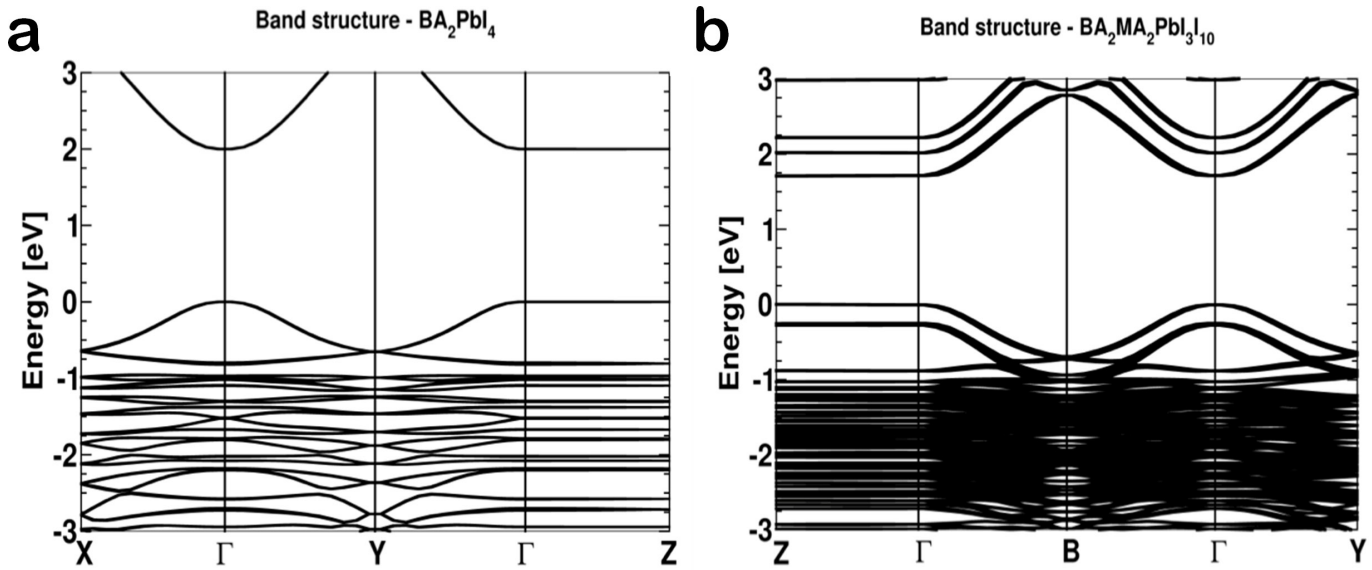

Extended Data Figure 3 | DFT computation. a, **b**, Electronic band structures of $(BA)_2PbI_4$ ($n = 1$; **a**) and $(BA)_2(MA)_2Pb_3I_{10}$ ($n = 3$; **b**) calculated using DFT with a local-density approximation, including the spin–orbit coupling and a bandgap correction computed using the HSE (Heyd–Scuseria–Ernzerhof) functional. The energy levels are referenced to the valence band maximum.

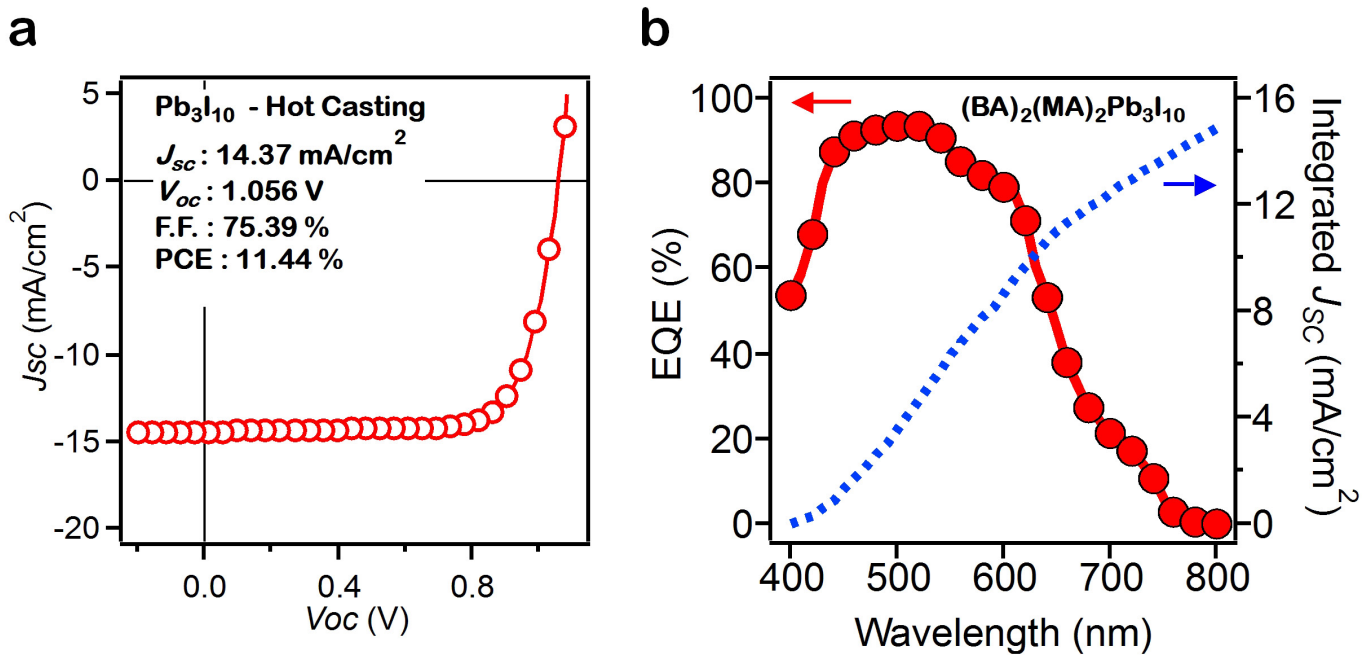

Extended Data Figure 4 | Device performance of $(BA)_2(MA)_2Pb_3I_{10}$. a, *J*–*V* curve and device parameters. **b**, EQE (red circles) and integrated J_{SC} from EQE (blue dashed line).

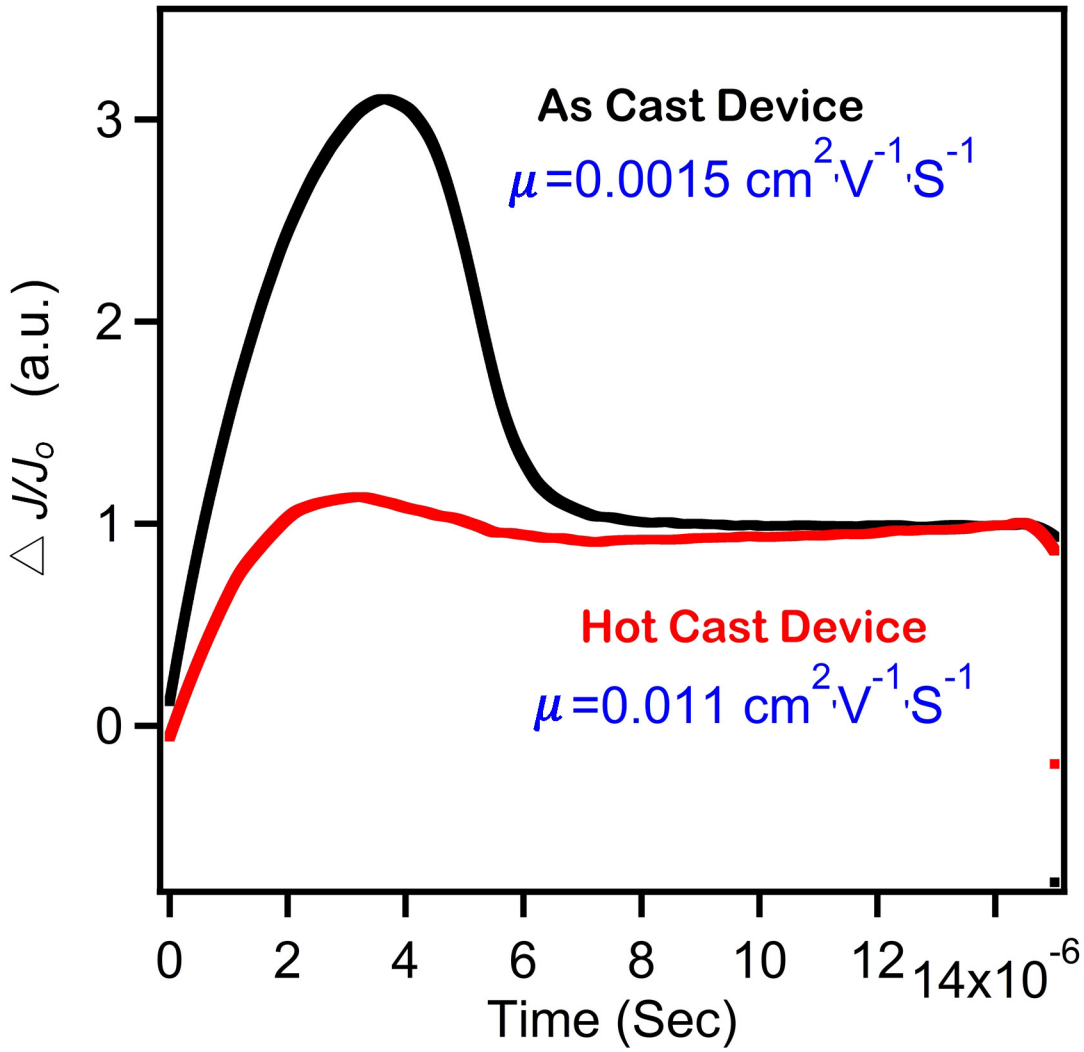

Extended Data Figure 5 | Dark current transient and mobility. The dark current transient ($\Delta J/J_0$), measured using the CELIV technique, for a hot-cast (red) and a room-temperature-cast ('As cast', black) device, and the mobility value (μ) in each case.

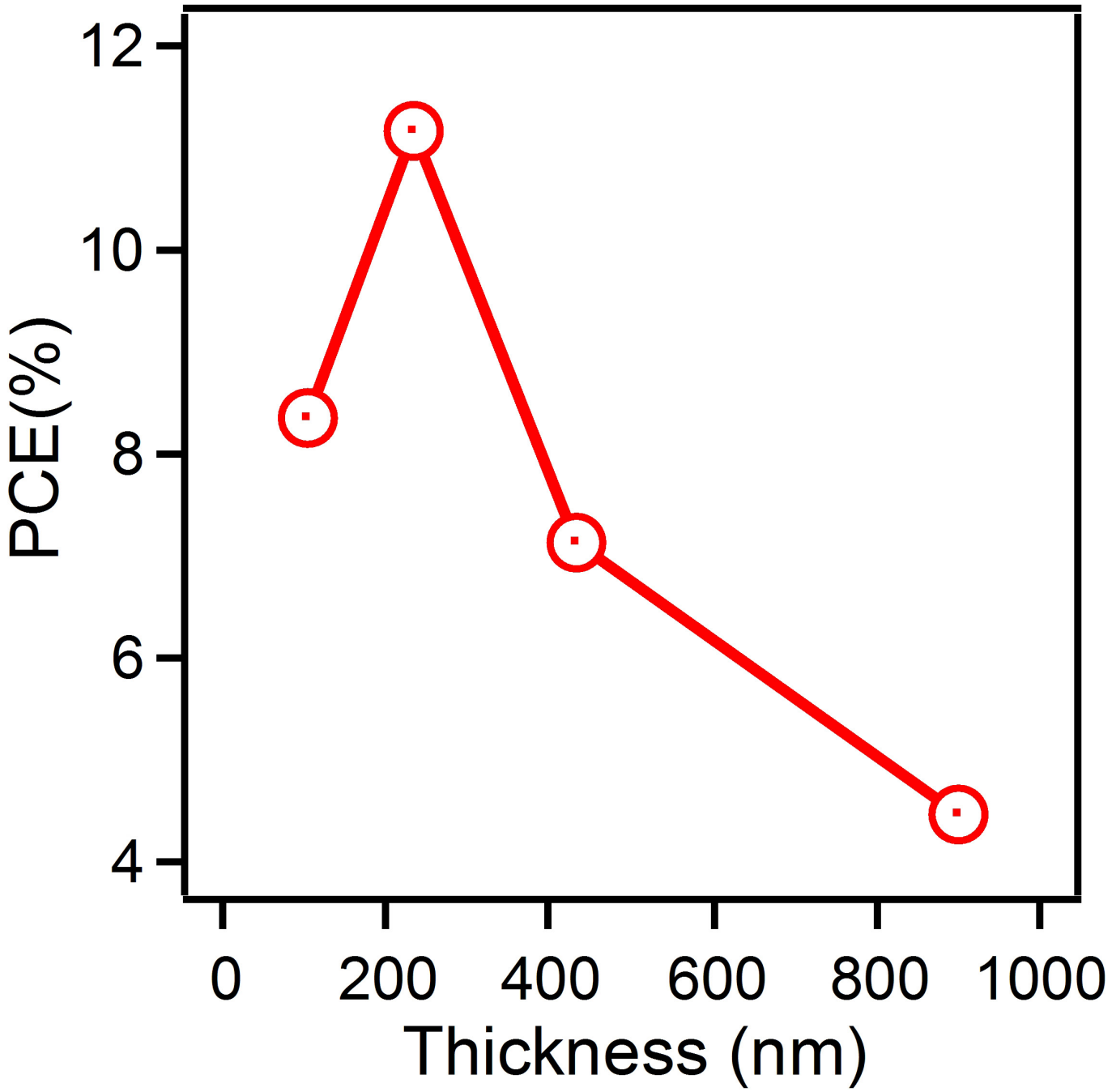

Extended Data Figure 6 | Device PCE as a function of thin-film thickness for the layered Pb_4I_{13} perovskite.

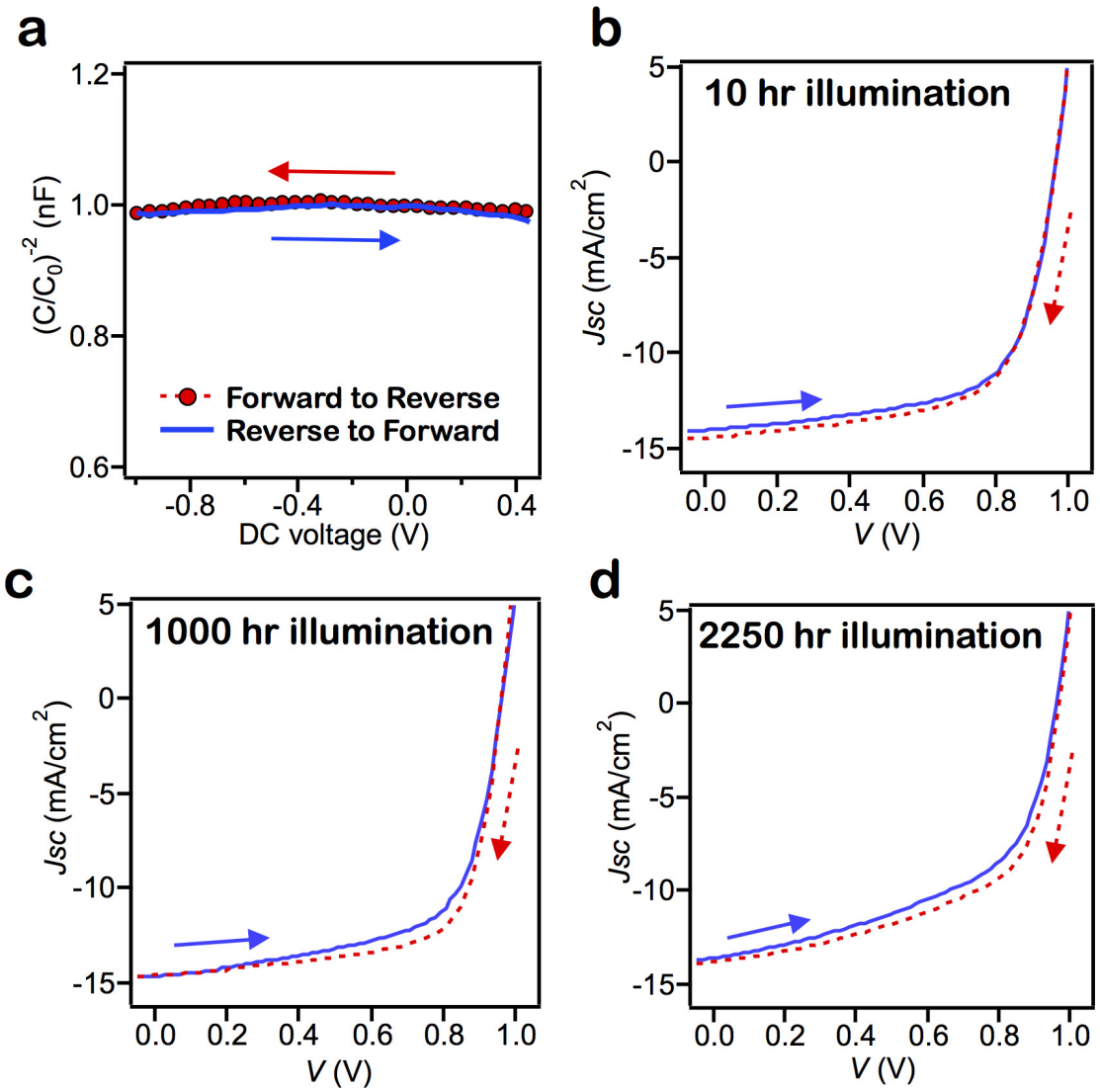

Extended Data Figure 7 | Hysteresis tests for 2D pervoskite devices. a–d, Tests with different bias sweep directions (**a**; $(C/C_0)^{-2}$ as function of DC bias, where C_0 is the capacitance of a geometric capacitor), and after 10 h (**b**), 1,000 h (**c**) and 2,250 h (**d**) of constant illumination. . The red and blue arrows indicate the forward and reverse sweep directions.

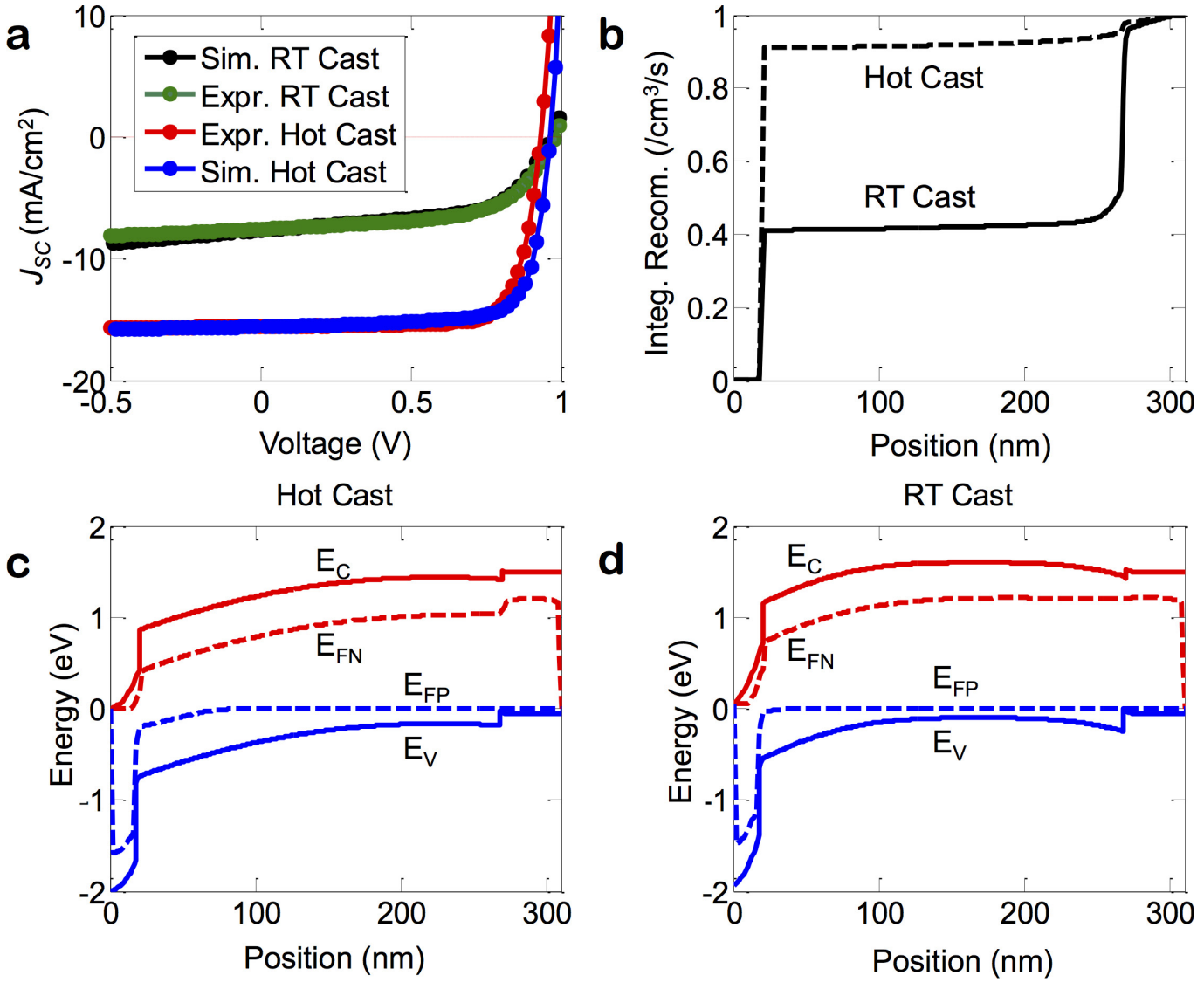

Extended Data Figure 8 | Simulation results and comparison of room-temperature-cast and hot-cast methods. a, Experimental ('Expr.') *J*–*V* characteristics of room-temperature-cast ('As cast') and hot-cast methods and corresponding simulation ('Sim.') results. The hot-cast method shows a current density with a larger magnitude and higher fill factor (area below the *J*–*V* curve). **b**, Integrated recombination inside three layers of a solar cell. Peak recombination shifts toward the PCBM/perovskite interface because the barrier for generated carriers is less in the hot-cast case than in the room-temperature-cast case. **c**, **d**, Energy band diagram of hot-cast (**c**) and room-temperature-cast (**d**) methods. Generated carriers face a lower barrier in the hot-cast case, especially close to the PEDOT/perovskite interface. E_C, conduction band; E_V, valence band; E_{FN}, electron quasi-Fermi level; E_{FP}, hole quasi-Fermi level.

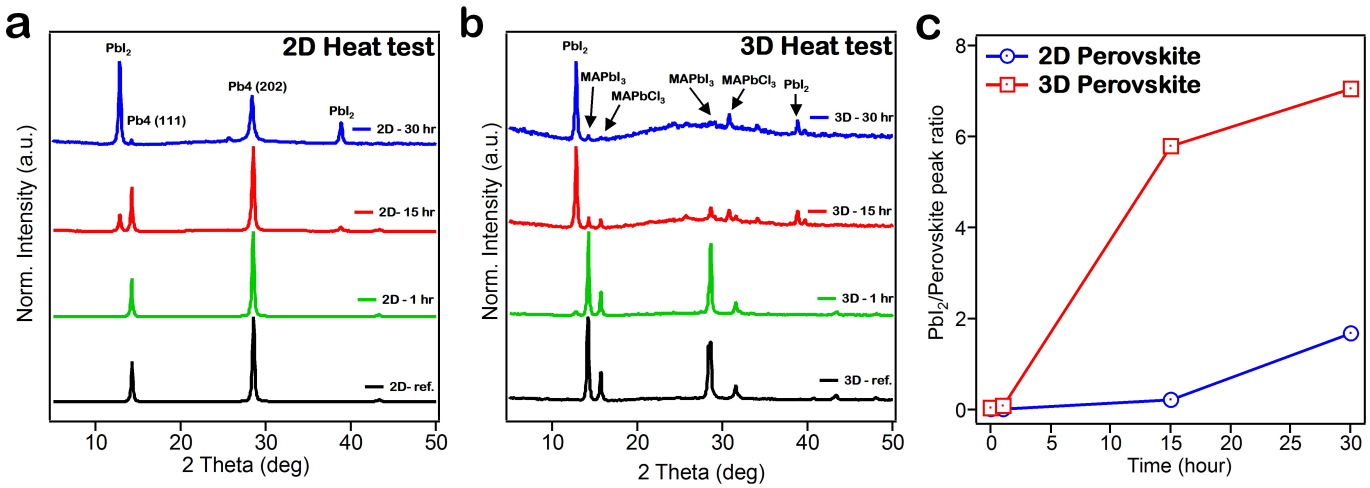

Extended Data Figure 9 | Heat stress tests. a, **b**, Spectra of 2D (**a**) and 3D (**b**) perovskite thin films under 80 °C in darkness after the lengths of time indicated (spectra are offset for clarity; 'ref.' refers to freshly made thin film, measured after 0 h of heat stressing). **c**, Ratio of the PbI_2 ($2\theta = 12.7°$) and perovskite ($2\theta = 14.2°$) main peaks in the spectra in **a** and **b** for the two perovskite materials (2D, blue; 3D, red) over 30 h of heating at 80 °C.